

First-principles Study of Non-Collinear Spin Fluctuations Using Self-adaptive Spin-constrained Method

Zefeng Cai,^{1,2,*} Ke Wang,² Yong Xu,³ Su-Huai Wei,⁴ and Ben Xu^{1,†}

¹*Graduate School of China Academy of Engineering Physics, Beijing 100088, People's Republic of China*

²*School of Materials Science and Engineering, Tsinghua University, Beijing 100084, People's Republic of China*

³*Department of Physics, Tsinghua University, Beijing 100084, People's Republic of China*

⁴*Beijing Computational Science Research Center, Beijing 100193, People's Republic of China*

(Dated: January 5, 2023)

Spin fluctuations have a substantial influence on the electron and lattice behaviors in magnetic materials, which, however, is difficult to be tracked properly by prevalent first-principles methods. We propose a versatile self-adaptive spin-constrained density functional theory formalism. Applying it to the simulation of itinerant ferromagnetic Fe, we present the potential energy surface comprising longitudinal and transverse variations of magnetization. Moreover, this method enables us to identify the delicate coupling between the magnetic moments and other degrees of freedom by following energy variation. As manifestations, magnetic interaction, electronic band structure, and phonon dispersion curves are illustrated for single-layered CrI₃ with excited magnetic configuration. All the above information can be obtained not only for spin fluctuations but also for non-collinear spin configurations with arbitrarily modulations; thus, it holds promise for future applications in condensed-matter physics research.

Spin fluctuations possess longitudinal and transverse perturbations of magnetic moments that deviate from ground-state magnetic configurations. They are crucial for determining the excited states and dynamic of magnetic systems, including the phase transition and transportation of electrons, phonons, and magnons. Further, spin fluctuations are prevalent in frustrated magnets [1–4], multiferroics [5–8], superconductors [9–19], topological magnets [20], etc, and are of crucial importance to phenomena such as superconductivity [9–19], quantum critical point [21–24], quantum phase transition [25], and the quantum anomalous Hall effect [26]. The above exotic phenomena stems from the delicate interaction between spin and other degree of freedoms (DoF) such as charge, orbital, and lattice. Despite the ubiquity of spin fluctuations, however, elucidation of the microscopic mechanism of these coupling effects is significantly challenging, due to the need of evaluating second or higher order derivatives of the energy with respect to the magnetic moment and other DoFs. In order to do so, the magnetic moment must be considered as a variable that can be altered independently from the other DoFs. And the manifestation of its variation, i.e. the excited magnetic states, is hence critical to understand the mutual interactions.

However, the commonly used density functional theory (DFT) [27] was originally developed to describe ground states. In their seminal works, Dederichs *et al.*[28] and Dudarev *et al.*[29, 30] introduced a Lagrange multiplier λ to constrain the magnetic moments when solving the Kohn-Sham equation as $\nabla_{\phi_i} L = 0$ [28, 29, 31–34]. However, it is difficult to simultaneously reach the global minimum of Lagrangian and meet the constraint, and thus it is not guaranteed that the magnetic moment \mathbf{M} gets to its constrained target. This situation is particularly se-

vere in itinerant metallic magnetic materials [35]. Therefore, the magnetic moment is difficult to control and to be considered as a completely independent DoF, and the energy of corresponding system is difficult to identify. These uncertainties escalate when the energy is differentiated by an infinitesimal variation of magnetic moment or other DoF, to evaluate the coupling strength, such as the magnetoelectrical coupling constant.

Another unfavorable fact is that these methods require the user to be highly proficient at interactively adjusting the optimization strategy [30, 34], which makes these methods highly prone to numerical error. This is because that the optimization is conducted only in the electronic energy functional minimization, where the constraining parameter λ is set as a pre-defined constant. λ , when improperly chosen, leads the system to a local minimum (λ too small) or to divergence (λ too big). In addition, this fixed λ is difficult to adapt to actual spin fluctuations where different magnetic components exhibit different deviations from the original ground state, which also makes the Hamiltonian numerically unstable to be diagonalized. Recently, Hegde *et al.*[36] developed a self-consistent method to impose spin constraints and sped up the convergence significantly. However, this method only deals with collinear magnetic orders, which hinder the study of complex noncollinear spin fluctuations.

To address these deficiencies, in this letter, we proposed a self-adaptive spin-constrained DFT scheme, where Kohn-Sham orbitals and the constraining vectors are updated iteratively to reach the global optimum of the Lagrangian and the target magnetic moments. In this scheme, the on-site adaptable constraint $\{\lambda_I\}$ are imposed in the form of a local vector field. The amplitude and orientation of the constraining vector field $\{\lambda_I\}$ depend on the local magnetic environment of atom

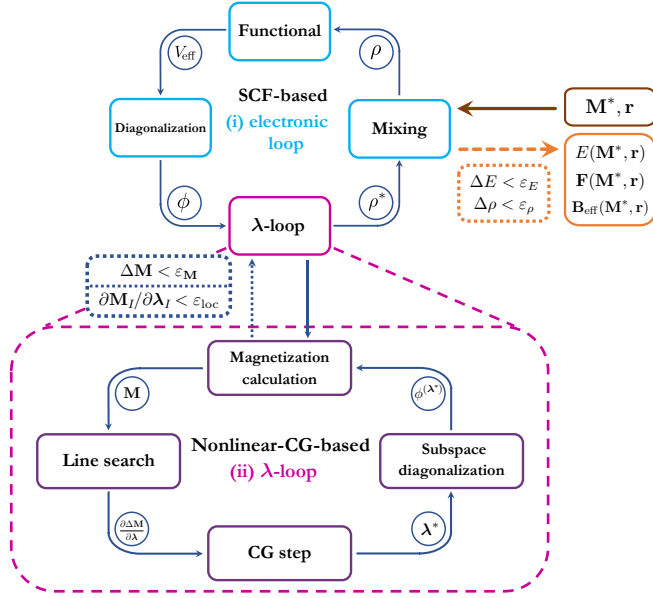


FIG. 1. Scheme of self-adaptive spin-constrained DFT method *DeltaSpin*. The outer electronic loop updates electron density ρ , while inner λ -loop updates constraining multiplier λ . (Subscripts for indexing atoms and orbitals are omitted for clarity.)

I and vary from component to component. Equipped with this strategy, the magnetic moment can be altered independently from the other DoFs in our non-collinear first-principles scheme. Our approach now paves the way for the investigation of spin fluctuation and its influence on other DoF. To exemplify this method, we then apply it to two scenarios. The first is a spin configuration with confined rotation, using ferromagnetic materials Fe and layered magnetic materials CrI₃ as examples. To simulate real-world fluctuations, it is later generalized to study the electronic band structure of CrI₃ with random magnetic orientations.

Our scheme is sketched in Fig. 1. It is based on the optimization of the Lagrangian function L under the constraint that the magnetic moment of atom I , that is, $\mathbf{M}_I(\{\phi_i\})$, is the same as the target value denoted by \mathbf{M}_I^* . To implement this, we design two nested loops updating the Kohn-Sham orbitals $\{\phi_i\}$ and the Lagrangian multiplier $\{\lambda_I\}$ respectively.

(i) *Electronic loop*: For a particular λ_I , we can solve

$$\frac{\delta E_{\text{KS}}}{\delta \langle \phi_i \rangle} - \sum_I \lambda_I \cdot \frac{\delta \mathbf{M}_I}{\delta \langle \phi_i \rangle} = \epsilon_i \langle \phi_i \rangle \quad (1)$$

to obtain a self-consistent solution $\{\phi_i(\lambda_I)\}$ and the magnetic moment $\mathbf{M}(\{\phi_i(\lambda_I)\})$. The atomic magnetic moment \mathbf{M}_I is generally defined as $\mathbf{M}_I(\{\phi_i\}) = \text{Tr}(\rho \sigma \hat{W}_I)$, where ρ is the density matrix, σ is the Pauli matrix, \hat{W}_I is a pre-defined weight operator for atom I .

Thus, Eq. 1 is obtained as

$$\hat{H}_{\text{KS}} |\phi_i\rangle - \sum_I \lambda_I \cdot \sigma \hat{W}_I |\phi_i\rangle = \epsilon_i |\phi_i\rangle. \quad (2)$$

Note that λ_I acts as a constraining field [28].

(ii) λ -loop: We can progressively update $\{\lambda_I\}$ by optimizing

$$\min_{\lambda_I} |\mathbf{M}(\{\phi_i(\lambda_I)\}) - \mathbf{M}^*|^2, \quad (3)$$

that is, the error $\Delta \mathbf{M}$ between the current magnetization and the target, using the nonlinear conjugate gradient (NCG) method. For an updated λ_I^* , we can solve Eq. 2 via diagonalization in the subspace spanned by the old orbitals $\{\phi_i(\lambda_I)\}$ to obtain a new set of orbitals $\{\phi_i(\lambda_I^*)\}$, and thus, the moment $\mathbf{M}(\lambda_I^*)$. In this way, the optimization can continue until a minimum is achieved. A perturbation-like scheme similar to that in Ref. [36] was chosen, which significantly reduced the computational cost compared to diagonalization in the entire basis set. In addition, the λ -loop converged rapidly because the function $\mathbf{M}(\{\phi_i(\lambda_I)\}) = \partial^2 L / \partial \lambda_I^2$ is proved to be almost monotonous according to the first-order perturbation theory ($L(\phi_i, \lambda_I, \epsilon_i)$ is a concave function of λ_I at 0 K [33]).

Certain details of the scheme deserve further discussion. In the λ -loop, the gradient of the object function can be approximated as $2(\mathbf{M}_I - \mathbf{M}_I^*) \frac{\partial \mathbf{M}_I}{\partial \lambda_I}$, based on the assumption that $\partial \mathbf{M}_I / \partial \lambda_I$, which is the non-local response to the on-site constraining field, is negligible. $\partial \mathbf{M}_I / \partial \lambda_I$ can be then obtained by lower-complexity estimation strategies for the NCG iteration. To provide better convergence, we control both $\Delta \mathbf{M} = \sqrt{|\mathbf{M}(\{\phi_i(\lambda_I)\}) - \mathbf{M}^*|^2}$ and the main diagonal of the gradients $\partial \mathbf{M}_I / \partial \lambda_I$ in the λ -loop. We first introduce a gradually tightened criterion ϵ_M for the former, preventing the constraining field from reaching an early stage local minimum. In case of the latter, the loop is programmed to stop when the local response was smaller than an empirical value ϵ_{loc} ($\epsilon_{\text{loc}} \approx 1 \mu_B^2 / \text{eV}$ works well across our limited tests). This criterion, which is based on the aforementioned localization assumption, is of particular importance. Additionally, the weight operator in Eq. 2 is often an integral in a real-space ball of radius r_{cut} with a smoothed boundary as $\hat{W}_I = \int d\mathbf{r} f(r_{\text{cut}} - |\mathbf{r} - \mathbf{r}_I|) |\mathbf{r}\rangle \langle \mathbf{r}|$. It may take a different form such as the Mulliken partitioning in atomic orbital basis DFT [37].

Upon convergence, the magnetic effective field can be obtained efficiently based on the Hellmann–Feynman theorem as

$$\mathbf{B}_I^{\text{eff}} = -\frac{\delta L(\mathbf{M}_I^*)}{\delta \mathbf{M}_I^*} = -\lambda_I. \quad (4)$$

This suggests that by continuously updating the constraining field, $\Delta \mathbf{M}$ is minimized and an increasingly

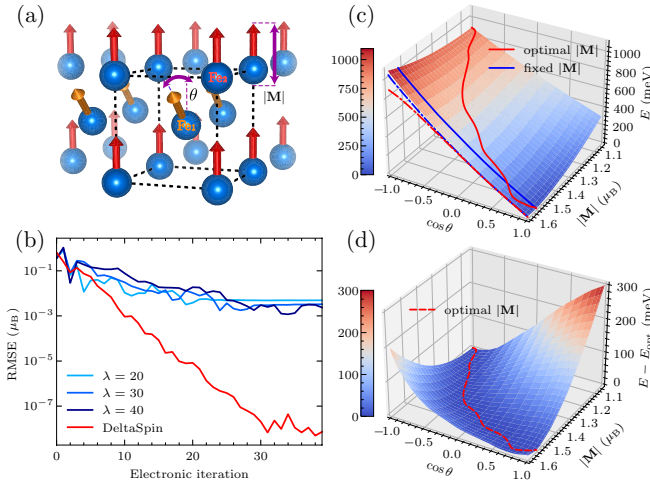


FIG. 2. Potential energy surface (PES) study of BCC iron with magnetic excitation. (a) Structure of BCC iron and spin configuration with deviated included angle of two neighboring Fe magnetic moments $\theta = \langle \mathbf{M}_{\text{Fe}1}, \mathbf{M}_{\text{Fe}2} \rangle$ and magnitude $|\mathbf{M}|$. (b) Comparison of convergence between *DeltaSpin* and former quadratic cDFT method with different λ . X axis: number of electronic iterations. Y axis: root-mean-square error (RMSE) between the obtained and the desired magnetization. (c) PES as a function of θ and $|\mathbf{M}|$. Solid and dashed lines respectively denote single-variable PES and its projection. Blue line indicates the PES with $|\mathbf{M}|$ fixed at ground-state value $1.54 \mu_B$ (using radial Bessel function as \hat{W}_I in Eq. 2). Red line indicates the PES with energy-minimized $|\mathbf{M}|$. Dashed lines are their projections. (d) PES relative to such energy-minimized path.

accurate estimation of the magnetic effective field is obtained, which turns out to be the constraining field λ_I itself. This estimation shows good correspondence with the true value, which is obtained via differentiation near the collinear limit, and a relative error of up to 4% through the entire path of non-collinear rotation (see Fig. S2 in the Supplementary Material [38]). This is because Eq. 4 is strictly correct only if $\langle \phi_i | \nabla_{\mathbf{M}_I} \hat{\mathcal{H}}_{\text{KS}} | \phi_i \rangle$ is negligible [39].

Potential Energy Surface A fine-grid potential energy surface (PES) is of great significance, particularly the one considering the spin DoF. While the previous quadratic cDFT requires a predetermined multiplier λ and may collapse during the early stage of the electronic loop (an analysis is presented in the Supplementary Material [38]), the proposed method can self-adaptively update the multiplier and exhibits a much better precision and efficiency. We studied the magnetic PES of the BCC iron (Fig. 2). The two DoFs scanned were the magnitude of atomic moments $|\mathbf{M}|$ and the included angle between the nearest neighbors' moments θ . In the calculations using former quadratic constraints, the root-mean-square error (RMSE) between the obtained and desired spin configurations were stuck at approximately $10^{-2} \mu_B$

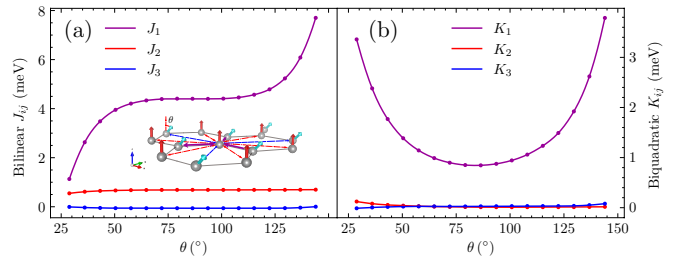


FIG. 3. Configuration dependency of bilinear and biquadratic exchange interaction in monolayer CrI₃. X axis: canting angle θ , that is, the included angle of two neighboring Cr magnetic moments. Y axis: the intensity of different exchange interactions. J_1 , J_2 , and J_3 represent the interaction between the first, second, and third nearest neighbors respectively (same with K_1 , K_2 , K_3 , indicated using different colors in the inset of (a)). (a) Bilinear parameter J_{ij} . The inset figure is an illustration of honeycomb CrI₃ and the exchange interaction where Cr atoms are denoted by grey balls and O atoms are omitted. (b) Biquadratic parameter K_{ij} .

(blue lines in Fig. 2(b)). In comparison, the *DeltaSpin* algorithm exhibited a much better convergence, where the RMSE decreased rapidly to nearly zero ($10^{-8} \mu_B$) for the same number of electronic iterations. We found that the energy-favored magnitude increased when the spins approached the ferromagnetic (FM) order and decreased when approaching anti-ferromagnetic (AFM) order. Moreover, the magnitude-optimized energy curve was the PES calculated using the former direction-only constraining method, which is a subset of our $V(|\mathbf{M}|, \theta)$ PES.

Effects on magnetic interactions One of the advantages of this method is the ability to obtain the real on-site magnetic interaction around an arbitrary magnetic configuration through simple calculations of the first derivative of energy E with respect to \mathbf{M} . This was not possible in previous studies as achieving precision for both E and $\delta\mathbf{M}$ was challenging. In Fig. 3, we show the calculated J_{ij} and K_{ij} as the bilinear exchange and biquadratic exchange parameters with variation in the magnetic configurations. The effective Hamiltonian used was $H = -\sum_{i,j>i} J_{ij} (\mathbf{e}_i \cdot \mathbf{e}_j) - \sum_{i,j>i} K_{ij} (\mathbf{e}_i \cdot \mathbf{e}_j)^2$, where i, j is the atom index. Both J_1 and K_1 exhibited strong dependency on the local magnetic configurations, as shown in Fig. 3. Further, J_1 from the previous energy-mapping strategy, which is a constant at approximately 3 meV [40], was between the maximum and the minimum of the result obtained.

Effects on lattice dynamics The variation in spin configuration has a non-trivial influence on phonon behaviors, and this study proposed a straightforward method to identify such couplings. This was performed by combining the frozen phonon method [41] with *DeltaSpin*. In particular, the system's energy must be precisely calculated at the atomic and magnetic excitations. Simulta-

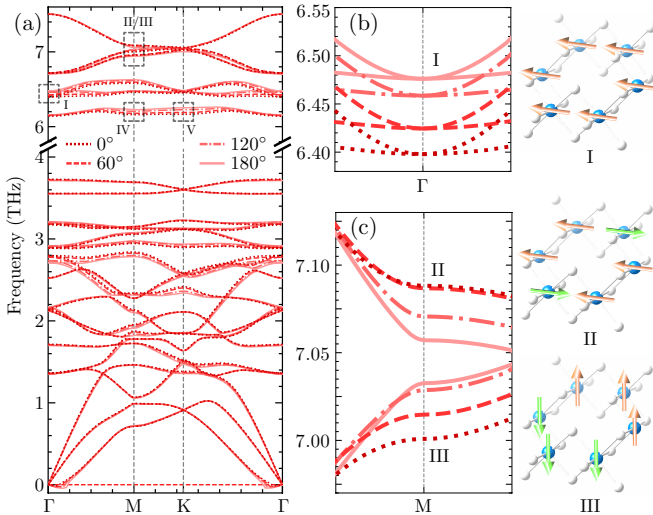


FIG. 4. Phonon structure of monolayer CrI_3 ’s different magnetic states. (a) Overall phonon spectrum at $\theta = 0^\circ, 60^\circ, 120^\circ, 180^\circ$. Dashed blocks indicate five modes (indexed by roman numerals) with significant frequency change owing to magnetic excitation. Physically-irreducible representations: I: $\Gamma_2^- + \Gamma_3^-$; II: M_1^- ; III: M_1^+ ; IV: M_1^+ ; V: K_1 . (b-c) Zoom image of mode I, II, and III with the schematic atomic displacement on the right side. Azure and white balls denote Cr and I atoms, respectively. The arrows indicate the instant direction of their motion, where the green and orange ones represent two opposite directions.

neously, the magnetic configuration must be prevented from “drifting away”. *DeltaSpin* can limit the energy and on-site moment error to 10^{-9} eV and $10^{-7} \mu_B$, respectively, while maintaining efficiency with more than one hundred atoms; to the best of our knowledge, it is the only method that can access this type of phonon calculations. Four selected spin-fluctuating states were obtained for CrI_3 (Fig. 4). Only the moments of chromium were constrained, while iodine atoms were fully relaxed, owing to the functionality of *DeltaSpin* to selectively constrain atoms or components. We found five modes that were significantly influenced by magnetic excitation, all of which appeared in the high-frequency branches where the Cr vibrations dominated (Fig. 4(a)). Regardless of spin-orbit coupling and anti-symmetric exchange, these frequency shifts can be roughly explained by the change in the “Heisenberg-only” force constant. $[\partial J_{ij}/\partial \mathbf{r}] [\mathbf{e}_i \cdot \mathbf{e}_j]$. The second term depends on the spin configuration explicitly. The first term, which is mainly contributed by the competition between the AFM t_{2g} - t_{2g} and FM t_{2g} - e_g interactions [42], also experiences considerable changes because of the different occupancies of e_g and t_{2g} orbitals across all four configurations. The existence of “collective-motion” modes, in which the distance between any two Cr atoms remains unchanged (Fig. 4(b), $\Gamma_2^- + \Gamma_3^-$), indicates that the interaction between Cr and I atoms, that is, the metal-ligand interaction, is also

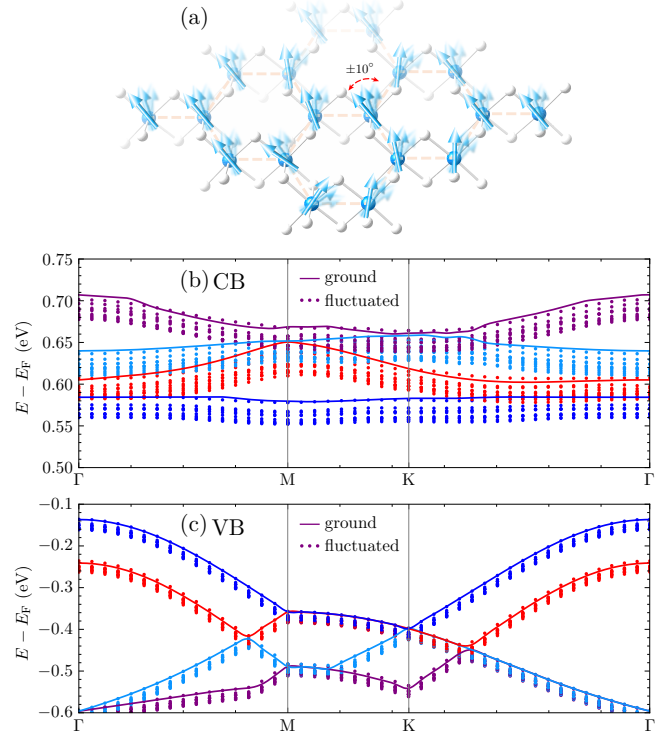


FIG. 5. Band dispersion near conduction band minimum (CBM) and valence band maximum (VBM), resulting from randomly fluctuated spin configurations. (a) Schematic of monolayer CrI_3 with randomly fluctuated spins. (b-c) Band dispersion for several selected branches. Solid curves represent ground-state bands while scatters represent corresponding fluctuated ones. Different colors are used to indicate different branches.

strongly affected by only changing the on-site moments of metal atoms. Moreover, the moments of I relax from $10^{-1} \mu_B$ to approximately zero as θ increases from 0° to 180° , whose importance has been demonstrated by previous research [43–46]. Using this algorithm, we can obtain the spin-lattice interaction information. Consequently, the process starts from the objective of obtaining a particular magnetic configuration to determine a feasible method of selective excitation via lattice vibrations. Thus, this can guide ultrafast THz experiments through resonant excitation of infrared (IR) [47] or Raman-active phonons [48].

Effects on Electronic Structure Spin fluctuations have a prominent effect on the electronic structure such as the band structure and orbital character of the Fermi surface [49–51]. First-principles calculations of electronic structures with spin fluctuations are a critical input for further evaluating the many-body effect [52]. Here, we demonstrate that the band structure is profoundly affected by spin fluctuations using the constrained method (Fig. 5). We modeled several spin-fluctuating configurations near the ground state of monolayer CrI_3 , wherein magnetic moments were drawn at random from the uniform distri-

bution within the FM order $\pm 10^\circ$. Their “excited” Kohn-Sham orbitals were then precisely calculated following the DFT routine, which distinguished our method from TDDFT utilizing the expansion of the ground state. Different branches from the obtained bands showed slightly different broadening behaviors with amplitudes varying in the range of 30–50 meV; consequently, the bandgap shifted. In addition, we obtained several electronic states with different canting angles θ in the transition from the FM to the Néel AFM phase of CrI_3 . These exhibited prominent variation in the band gap, Fermi surface, and topological features (see Fig. S4–5 in the Supplementary Material [38]). Thus, this method can be a potentially useful strategy to access a spin-renormalized band structure that fully considers the coupling between spin and electronic DoF [11], which is exceptionally useful for investigating fundamental low-energy physics or exploring rich functionalities in dynamic or optical properties.

This study proposes a self-adaptive spin-constrained DFT method wherein the spin fluctuations or magnetic excitation were incorporated along with spin-orbit coupling and non-collinear magnetic configurations, capable of dealing with full degrees of freedom of the amplitude and rotation angle from both magnetic and ligand atoms [46]. This enabled us to gain further insight into spin fluctuations from the electron, lattice, and magnetic perspectives, and also get access to the wave function of magnetic excited states. Here we demonstrate the broadening of band because of the random perturbations of magnetic moments, while this can be easily scaled to different temperature and the broadening with k dependence can be an indicator to real coupling between spin and other DoFs such as electron and lattice. In addition, the obtained precise atomic forces and magnetic effective fields could be employed as the driving forces in further dynamical simulations such as Landau–Lifshitz–Gilbert (or Landau–Lifshitz–Bloch) or TDDFT [53, 54]. Moreover, the rapid calculation of energy and its corresponding derivatives indicate its ability as a systematic data generator for machine learning surrogate models [55–59] and is expected to be revolutionary with its ability to obtain arbitrary spin-lattice configurations with first-principles precision and high efficiency.

We appreciate Han Wang, Kun Cao, C. Freysoldt for their helpful discussions. This work was funded by the National Natural Science Foundation of China (Grant Nos. 51790494 and 12088101).

- [2] A. Pelissetto and E. Vicari, Critical phenomena and renormalization-group theory, *Physics Reports* **368**, 549 (2002).
- [3] L. Balents, Spin liquids in frustrated magnets, *Nature* **464**, 199 (2010).
- [4] C. Nisoli, R. Moessner, and P. Schiffer, Colloquium: Artificial spin ice: Designing and imaging magnetic frustration, *Rev. Mod. Phys.* **85**, 1473 (2013).
- [5] Y. Tokura, S. Seki, and N. Nagaosa, Multiferroics of spin origin, *Reports on Progress in Physics* **77** (2014).
- [6] H. J. Xiang, S.-H. Wei, M.-H. Whangbo, and J. L. F. Da Silva, Spin-orbit coupling and ion displacements in multiferroic TbMnO_3 , *Phys. Rev. Lett.* **101**, 037209 (2008).
- [7] X. Fabrèges, S. Petit, I. Mirebeau, S. Pailhès, L. Pinsard, A. Forget, M. T. Fernandez-Diaz, and F. Porcher, Spin-lattice coupling, frustration, and magnetic order in multiferroic RMnO_3 , *Phys. Rev. Lett.* **103**, 067204 (2009).
- [8] S. Lee, A. Pirogov, J. H. Han, J.-G. Park, A. Hoshikawa, and T. Kamiyama, Direct observation of a coupling between spin, lattice and electric dipole moment in multiferroic ymno_3 , *Phys. Rev. B* **71**, 180413 (2005).
- [9] P. W. Anderson, Heavy-electron superconductors, spin fluctuations, and triplet pairing, *Phys. Rev. B* **30**, 1549 (1984).
- [10] Y. Sidis, M. Braden, P. Bourges, B. Hennion, S. NishiZaki, Y. Maeno, and Y. Mori, Evidence for incommensurate spin fluctuations in Sr_2RuO_4 , *Phys. Rev. Lett.* **83**, 3320 (1999).
- [11] T. Kuwabara and M. Ogata, Spin-triplet superconductivity due to antiferromagnetic spin-fluctuation in Sr_2RuO_4 , *Phys. Rev. Lett.* **85**, 4586 (2000).
- [12] I. I. Mazin and D. J. Singh, Ferromagnetic spin fluctuation induced superconductivity in Sr_2RuO_4 , *Phys. Rev. Lett.* **79**, 733 (1997).
- [13] J. M. Tranquada, W. J. L. Buyers, H. Chou, T. E. Mason, M. Sato, S. Shamoto, and G. Shirane, Spin fluctuations in superconducting $\text{YBa}_2\text{Cu}_3\text{O}_{6.5}$, *Phys. Rev. Lett.* **64**, 800 (1990).
- [14] P. Monthoux and D. Pines, Spin-fluctuation-induced superconductivity in the copper oxides: A strong coupling calculation, *Phys. Rev. Lett.* **69**, 961 (1992).
- [15] H. A. Mook, P. Dai, S. M. Hayden, G. Aeppli, T. G. Perring, and F. Doğan, Spin fluctuations in $\text{YBa}_2\text{Cu}_3\text{O}_{6.6}$, *Nature* **395**, 580 (1998).
- [16] M. D. Lumsden, A. D. Christianson, E. A. Goremychkin, S. E. Nagler, H. A. Mook, M. B. Stone, D. L. Abernathy, T. Guidi, G. J. MacDougall, C. de la Cruz, A. S. Sefat, M. A. McGuire, B. C. Sales, and D. Mandrus, Evolution of spin excitations into the superconducting state in $\text{FeTe}_{1-x}\text{Se}_x$, *Nature Physics* **6**, 182 (2010).
- [17] T. Chen, Y. Chen, A. Kreisel, X. Lu, A. Schneidewind, Y. Qiu, J. T. Park, T. G. Perring, J. R. Stewart, H. Cao, R. Zhang, Y. Li, Y. Rong, Y. Wei, B. M. Andersen, P. J. Hirschfeld, C. Broholm, and P. Dai, Anisotropic spin fluctuations in detwinned FeSe , *Nature Materials* **18**, 709 (2019).
- [18] T. Moriya and K. Ueda, Spin fluctuations and high temperature superconductivity, *Advances in Physics* **49**, 555 (2000).
- [19] T. Moriya and K. Ueda, Antiferromagnetic spin fluctuation and superconductivity, *Reports on Progress in Physics* **66**, 1299 (2003).
- [20] J. Li, Y. Li, S. Du, Z. Wang, B.-L. Gu, S.-C. Zhang,

* caizf21@mails.tsinghua.edu.cn

† bxu@gsc.aep.ac.cn

[1] S.-H. Lee, C. Broholm, W. Ratcliff, G. Gasparovic, Q. Huang, T. H. Kim, and S.-W. Cheong, Emergent excitations in a geometrically frustrated magnet, *Nature* **418**, 856 (2002).

K. He, W. Duan, and Y. Xu, Intrinsic magnetic topological insulators in van der waals layered MnBi₂Te₄-family materials, *Science Advances* **5**, eaaw5685 (2019).

[21] A. Rosch, Interplay of disorder and spin fluctuations in the resistivity near a quantum critical point, *Phys. Rev. Lett.* **82**, 4280 (1999).

[22] A. Georges, O. Parcollet, and S. Sachdev, Quantum fluctuations of a nearly critical heisenberg spin glass, *Phys. Rev. B* **63**, 134406 (2001).

[23] K. Ishida, K. Okamoto, Y. Kawasaki, Y. Kitaoka, O. Trovarelli, C. Geibel, and F. Steglich, YbRh₂Si₂: Spin fluctuations in the vicinity of a quantum critical point at low magnetic field, *Phys. Rev. Lett.* **89**, 107202 (2002).

[24] H. v. Löhneysen, A. Rosch, M. Vojta, and P. Wölfle, Fermi-liquid instabilities at magnetic quantum phase transitions, *Rev. Mod. Phys.* **79**, 1015 (2007).

[25] J. Zhang, C.-Z. Chang, P. Tang, Z. Zhang, X. Feng, K. Li, L. li Wang, X. Chen, C. Liu, W. Duan, K. He, Q.-K. Xue, X. Ma, and Y. Wang, Topology-driven magnetic quantum phase transition in topological insulators, *Science* **339**, 1582 (2013).

[26] Y.-H. Li and R. Cheng, Spin fluctuations in quantized transport of magnetic topological insulators, *Phys. Rev. Lett.* **126**, 026601 (2021).

[27] W. Kohn and L. J. Sham, Self-consistent equations including exchange and correlation effects, *Physical review* **140**, A1133 (1965).

[28] P. H. Dederichs, S. Blügel, R. Zeller, and H. Akai, Ground states of constrained systems: Application to cerium impurities, *Phys. Rev. Lett.* **53**, 2512 (1984).

[29] P.-W. Ma and S. L. Dudarev, Constrained density functional for noncollinear magnetism, *Phys. Rev. B* **91**, 054420 (2015).

[30] S. L. Dudarev, P. Liu, D. A. Andersson, C. R. Stanev, T. Ozaki, and C. Franchini, Parametrization of LSDA+U for noncollinear magnetic configurations: Multipolar magnetism in UO₂, *Phys. Rev. Materials* **3**, 083802 (2019).

[31] M. Richter, U. Nitzsche, and H. Eschrig, Constrained density functional calculations for magnetic systems, *Journal of Magnetism and Magnetic Materials* **140-144**, 207 (1995), international Conference on Magnetism.

[32] G. M. Stocks, B. Ujfaluassy, X. Wang, D. M. C. Nicholson, W. A. Shelton, Y. Wang, A. Canning, and B. L. Györfy, Towards a constrained local moment model for first principles spin dynamics, *Philosophical Magazine B* **78**, 665 (1998).

[33] Q. Wu and T. Van Voorhis, Direct optimization method to study constrained systems within density-functional theory, *Phys. Rev. A* **72**, 024502 (2005).

[34] P. Kurz, F. Förster, L. Nordström, G. Bihlmayer, and S. Blügel, Ab initio treatment of noncollinear magnets with the full-potential linearized augmented plane wave method, *Physical Review B* **69**, 024415 (2004).

[35] B. Zimmermann, G. Bihlmayer, M. Böttcher, M. Bouhas-soune, S. Lounis, J. Sinova, S. Heinze, S. Blügel, and B. Dupé, Comparison of first-principles methods to extract magnetic parameters in ultrathin films: Co/Pt(111), *Phys. Rev. B* **99**, 214426 (2019).

[36] O. Hegde, M. Grabowski, X. Zhang, O. Waseda, T. Hickel, C. Freysoldt, and J. Neugebauer, Atomic relaxation around defects in magnetically disordered materials computed by atomic spin constraints within an efficient lagrange formalism, *Phys. Rev. B* **102**, 144101 (2020).

[37] R. Cuadrado, M. Pruneda, A. García, and P. Ordejón, Implementation of non-collinear spin-constrained DFT calculations in siesta with a fully relativistic hamiltonian, *Journal of Physics: Materials* **1**, 015010 (2018).

[38] See Supplemental Material for discussions on previous Lagrangian-based constraining method, calculations of spin spirals and magnetic torques, and more details about exchange parameter fitting and topological electronic structure under spin fluctuations.

[39] S. Streib, V. Borisov, M. Pereiro, A. Bergman, E. Sjöqvist, A. Delin, O. Eriksson, and D. Thonig, Equation of motion and the constraining field in ab initio spin dynamics, *Phys. Rev. B* **102**, 214407 (2020).

[40] L. Ke and M. I. Katsnelson, Electron correlation effects on exchange interactions and spin excitations in 2d van der waals materials, *npj Computational Materials* **7**, 1 (2021).

[41] A. Togo and I. Tanaka, First principles phonon calculations in materials science, *Scr. Mater.* **108**, 1 (2015).

[42] B. Sadhukhan, A. Bergman, Y. O. Kvashnin, J. Hellsvik, and A. Delin, Spin-lattice couplings in two-dimensional CrI₃ from first-principles computations, *Phys. Rev. B* **105**, 104418 (2022).

[43] M. Ye and D. Vanderbilt, Dynamical magnetic charges and linear magnetoelectricity, *Phys. Rev. B* **89**, 064301 (2014).

[44] M. Ye and D. Vanderbilt, Magnetic charges and magnetoelectricity in hexagonal rare-earth manganites and ferrites, *Phys. Rev. B* **92**, 035107 (2015).

[45] R. Logemann, A. N. Rudenko, M. I. Katsnelson, and A. Kirilyuk, Exchange interactions in transition metal oxides: the role of oxygen spin polarization, *Journal of Physics: Condensed Matter* **29**, 335801 (2017).

[46] I. V. Solov'yev, Exchange interactions and magnetic force theorem, *Phys. Rev. B* **103**, 104428 (2021).

[47] S. Foteinopoulou, G. C. R. Devarapu, G. S. Subramania, S. Krishna, and D. Wasserman, Phonon-polaritonics: enabling powerful capabilities for infrared photonics, *Nanophotonics* **8**, 2129 (2019).

[48] M. Forst, R. Mankowsky, and A. Cavalleri, Mode-selective control of the crystal lattice, *Accounts of chemical research* **48**, 380 (2015).

[49] T. A. Maier, S. Graser, P. J. Hirschfeld, and D. J. Scalapino, *d*-wave pairing from spin fluctuations in the K_xFe_{2-y}Se₂ superconductors, *Phys. Rev. B* **83**, 100515 (2011).

[50] L. Fanfarillo, J. Mansart, P. Toulemonde, H. Cercellier, P. Le Fevre, F. Bertran, B. Valenzuela, L. Benfatto, and V. Brouet, Orbital-dependent fermi surface shrinking as a fingerprint of nematicity in FeSe, *Physical Review B* **94**, 155138 (2016).

[51] L. C. Rhodes, M. D. Watson, A. A. Haghaghian, D. V. Evtushinsky, M. Eschrig, and T. K. Kim, Scaling of the superconducting gap with orbital character in FeSe, *Phys. Rev. B* **98**, 180503 (2018).

[52] K. Held, I. Nekrasov, G. Keller, V. Eyert, N. Blümer, A. McMahan, R. Scalettar, T. Pruschke, V. Anisimov, and D. Vollhardt, Realistic investigations of correlated electron systems with LDA+DMFT, *physica status solidi (b)* **243**, 2599 (2006).

[53] D. A. Garanin, Fokker-planck and landau-lifshitz-bloch equations for classical ferromagnets, *Phys. Rev. B* **55**, 3050 (1997).

[54] T. L. Gilbert, A phenomenological theory of damping in

ferromagnetic materials, *IEEE transactions on magnetics* **40**, 3443 (2004).

[55] I. Novikov, B. Grabowski, F. Kormann, and A. Shapeev, Machine-learning interatomic potentials reproduce vibrational and magnetic degrees of freedom, *arXiv preprint arXiv:2012.12763* (2020).

[56] J. Tranchida, S. Plimpton, P. Thibaudeau, and A. Thompson, Massively parallel symplectic algorithm for coupled magnetic spin dynamics and molecular dynamics, *Journal of Computational Physics* **372**, 406 (2018).

[57] S. Nikolov, M. A. Wood, A. Cangi, J.-B. Maillet, M.-C. Marinica, A. P. Thompson, M. P. Desjarlais, and J. Tranchida, Data-driven magneto-elastic predictions with scalable classical spin-lattice dynamics, *npj Computational Materials* **7**, 153 (2021).

[58] M. Eckhoff and J. Behler, High-dimensional neural network potentials for magnetic systems using spin-dependent atom-centered symmetry functions, *npj Computational Materials* **7**, 1 (2021).

[59] H. Yu, C. Xu, X. Li, F. Lou, L. Bellaiche, Z. Hu, X. Gong, and H. Xiang, Complex spin hamiltonian represented by an artificial neural network, *Phys. Rev. B* **105**, 174422 (2022).

Supplementary Material: First-principles Study of Non-Collinear Spin Fluctuations Using Self-adaptive Spin-constrained Method

Zefeng Cai,^{1,2,*} Ke Wang,² Yong Xu,³ Su-Huai Wei,⁴ and Ben Xu^{1,†}

¹*Graduate School of China Academy of Engineering Physics,
Beijing 100088, People's Republic of China*

²*School of Materials Science and Engineering,
Tsinghua University, Beijing 100084, People's Republic of China*

³*Department of Physics, Tsinghua University,
Beijing 100084, People's Republic of China*

⁴*Beijing Computational Science Research Center,
Beijing 100193, People's Republic of China*

(Dated: January 5, 2023)

A. Analysis of λ -fixed spin constraining methods and comparison with the self-adaptive spin-constrained method (DeltaSpin)

In previous cDFT [1] method, a fixed multiplier λ is introduced into the Lagrangian of the system, which takes the form of

$$L(\{\phi_i\}, \lambda, \{\eta_i\}) = E_{\text{KS}}[\{\phi_i\}] - \sum_i \eta_i [\langle \phi_i | \phi_j \rangle - \delta_{ij}] + \lambda \sum_I [\mathbf{M}_I(\{\phi_i\}) - \mathbf{M}_I^*]^2. \quad (1)$$

The constraining potential, which can be obtained by taking variational derivatives with respect to orbitals ϕ_i , carries the pre-factor of $2\lambda \sum_I (\mathbf{M}_I - \mathbf{M}_I^*)$. The optimization of this Lagrangian function is performed merely by electronic minimization, that is, self-consistently solving ϕ_i , where λ is set as a constant.

Several factors can sabotage this process. Firstly, the fixed λ makes the Hamiltonian unstable to be diagonalized particularly when the initial moments are far from the target (large $2\lambda \sum_I (\mathbf{M}_I - \mathbf{M}_I^*)$), and ending up with rough precision. Although one can achieve fair convergence by setting small λ at an early stage and gradually increasing it, the process is purely empirical and oversimplified. Secondly, every component of every magnetic moment does not share the same λ in the real cases of spin fluctuations. Each magnetic component exhibits different deviation from the original ground state, which obviously requires that the constraining field λ depends on the local magnetic environment and varies from component to component. Furthermore, the Jacobian matrix of constraint condition has all-zero entries ($2(\mathbf{M}_I - \mathbf{M}_I^*) \frac{\partial \mathbf{M}_I}{\partial \phi_i}$) when every $\mathbf{M}_I = \mathbf{M}_I^*$, which makes the quadratic penalty a theoretically, to be more specific, rank-wisely illegal constraint for determining the target minimum via Lagrangian multiplier formalism.

The following tests proved that the total energy obtained using DeltaSpin can be viewed as the limit of those using λ -fixed methods as λ tends to $+\infty$, which is inaccessible owing to numerical instability of λ -fixed methods (see Tab. S1).

* caizf21@mails.tsinghua.edu.cn

† bxu@gscap.ac.cn

TABLE S1. Total energy of a non-ground state constrained using VASP and DeltaSpin.

Method	λ	E ^a		RMSE ^b (μ_B)
		(eV)	(μ_B)	
VASP	10	-16.91540089	3.98×10^{-3}	
	30	-16.91496141	1.36×10^{-4}	
	40	-16.91490396	1.02×10^{-4}	
	45	-16.91488467	0.91×10^{-4}	
	50 ^c	—	—	
DeltaSpin	—	-16.91472775	1.18×10^{-8}	

^a The energy from VASP has already been subtracted by

$$E_{\text{penalty}} = \lambda \sum_I [\mathbf{M}_I(\{\phi_i\}) - \mathbf{M}_I^*]^2.$$

^b Root mean square error between obtained and target on-site magnetic moments.

^c Diagonalization crashed due to excessive multiplier λ .

B. Comparison of constraint-free spin-fluctuating states obtained with and without Lagrangian-based constraints

Certain non-collinear spin-fluctuating states can be obtained using first-principles approaches without imposing explicit constraints. Spin spiral, for example, may be conveniently modeled using a generalization of the Bloch condition. While the size of the system, that is, the number of atoms or the volume of the cell, can be the same as the ground state if using this means, the appropriate cutoff energy of the basis set may become considerably larger. Alternatively, we can also model spin spiral as a non-collinear magnetic configuration with a unusual periodicity along propagation vector, and then conduct a self-consistent DFT routine while maintaining such configuration, which can be easily done using DeltaSpin.

We obtained several spin spirals in FCC iron using these two different approaches. The propagation vector \mathbf{q} pointed in the direction of $(0\ 0\ 1)$ with $|\mathbf{q}|$ ranging from 0 to 1. The energy-minimized magnitude of the spins decreased remarkably as $|\mathbf{q}|$ went from 0 to 1. Using DeltaSpin, we calculated the total energy while constraining the spin moments at their energy-favored magnitude (red curve), which exhibited a good correspondence with

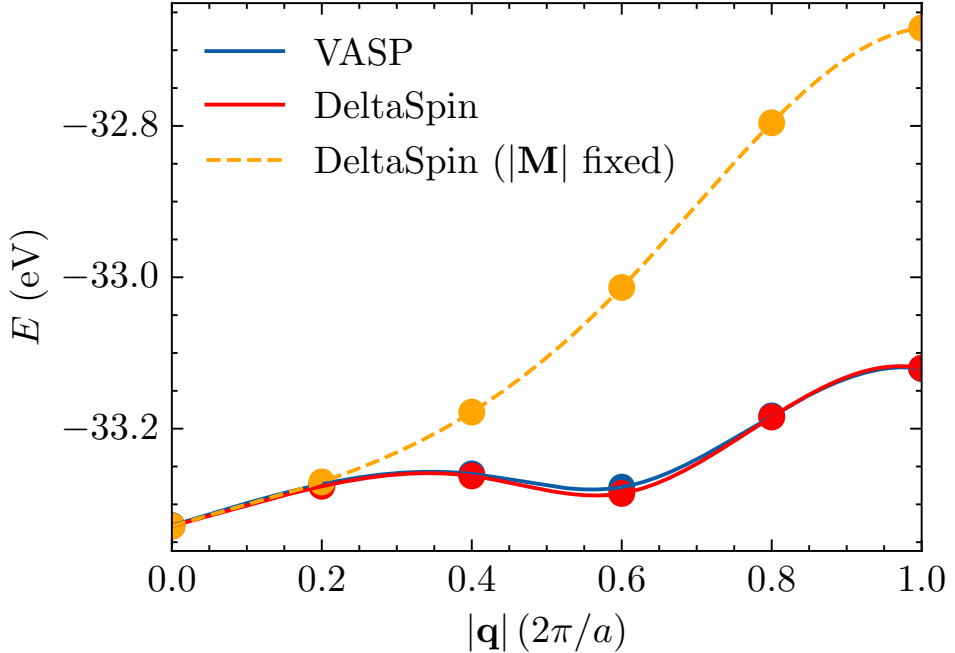


FIG. S1. Total energy of spin spiral in FCC iron calculated using generalized Bloch condition and DeltaSpin, respectively. \mathbf{q} points in the direction of $(0\ 0\ 1)$. $|\mathbf{q}|$ ranges from 0 to 1 with $2\pi/a$ as the unit. a denotes the lattice constant of FCC iron.

that from the constraint-free approach (blue curve), and at a fixed $1.7805\ \mu_B$ (orange dash), which was its magnitude at $|\mathbf{q}| = 0$, that is, FM order. These results demonstrate the accuracy and versatility of self-adaptive spin-constrained method DeltaSpin.

C. Two different strategies to calculate magnetic torques using DeltaSpin

There are two different strategies to calculate magnetic effective fields $\frac{\delta E}{\delta \mathbf{M}}$ and magnetic torques $\frac{\delta E}{\delta \mathbf{e}}$, which could be employed as the driving forces in further dynamical simulations using real-time TDDFT or the Landau-Lifshitz-Gilbert(Bloch) method. (i) Finite difference approximation directly using the definition, that is, taking derivatives of the total energy E with respect to \mathbf{M}_I^* ; (ii) Hellmann–Feynman approximation, explained in the main text.

We compared such constraining-field-approximated magnetic torques to the finite-differentiated ones in BCC iron and monolayer CrI₃ (see Fig. S2). The maximum relative error was about 4%, which was attributed to the non-collinear contribution in Kohn-Sham functional $\langle \phi_i | \nabla_{\mathbf{M}_I} \hat{\mathcal{H}}_{\text{KS}} | \phi_i \rangle$, and perfectly acceptable in some cases. Notice that the dif-

ference was negligible in the collinear limit, that is, in the neighborhood of FM and AFM order, both in Fe and in CrI₃.

Hellmann–Feynman approximation is a efficient and reliable choice given that the complexity of explicit differentiation is at least $\mathcal{O}(N)$ (N is the number of atoms) whereas to obtain constraining field only one calculation is needed. In addition, if a delicate description instead of a crude estimate of magnetic dynamics is needed, one can always apply an infinitesimal change to spin moments, recalculate the total energy, and take the derivatives. This procedure is also unachievable for λ -fixed constraining formalism wherein the inadequate precision of energy leads to poor precision of magnetic torques.

D. More details of magnetic interaction parameter fitting

Inspired by the energy-mapping method [2], we defined “canting angle” θ in honeycomb-like MX₃ as Fig. S3. We fit a “local” second-order polynomial around θ^* to the total energy of certain configurations with different θ as follows:

$$H = - \sum_{i < j} J_{ij} (\hat{\mathbf{e}}_i \cdot \hat{\mathbf{e}}_j) - \sum_{i < j} K_{ij} (\hat{\mathbf{e}}_i \cdot \hat{\mathbf{e}}_j)^2 \quad (2)$$

$$= a_0(\theta^*) + a_1(\theta^*) \cdot \cos \theta + a_2(\theta^*) \cdot \cos^2 \theta, \quad (3)$$

where θ is in the neighborhood of θ^* , that is, $\theta \in (\theta^* - \delta\theta, \theta^* + \delta\theta)$. Notice that all coefficients of the polynomial implicitly depends on the centered θ^* .

After deduction, θ^* -centered pair-wise exchange parameters from the first nearest neighbor (1-NN) up to 3-NN can be solved via

$$\begin{pmatrix} 6 & 0 & 6 \\ 2 & 8 & 6 \\ 4 & 8 & 0 \end{pmatrix} \begin{pmatrix} J_1, K_1 \\ J_2, K_2 \\ J_3, K_3 \end{pmatrix} = - \begin{pmatrix} a_1^N, a_2^N \\ a_1^Z, a_2^Z \\ a_1^S, a_2^S \end{pmatrix}, \quad (4)$$

where the dependency of all quantities on θ^* are omitted. N for Néel, Z for Zigzag, S for Stripy. These exchange parameters can be treated as the local exchange parameters at θ^* .

E. More details of electronic structure under spin fluctuations

The wave function is solved precisely via DeltaSpin for spin-fluctuating states. Thus, we are able to depict more detailed electronic structure. Strong interplay between mag-

netism and topology of electronic states was found, bringing forth rich functionalities in dynamical or optical properties. The topological sensibility to the magnetic configuration was observed for the first time using cDFT. We modeled ten excited states with different canting angles θ in the transition from FM to Néel AFM phase of monolayer CrI₃. They exhibited significant variation in band structure, band gap, and Fermi surface as shown in Fig. S4. We noticed the splitting of every two-fold degenerate band when θ went from 180° to 0°, following the parity-time (PT) symmetry breaking from AFM to FM phase. It could be further demonstrated in Fermi surface, where one hexagon-shape band in AFM phase split into two concentric circle-shaped valence bands in FM phase (Fig. S4(c)). This process happened on Γ -M path first, then on Γ -K. Simultaneously, the band gap went through a variation of about 50 meV. Moreover, we demonstrated the change of Berry curvature $\mathbf{F}(\mathbf{k})$ and its sensitivity $\partial\mathbf{F}(\mathbf{k})/\partial\theta$ in the process (see Fig. S5), which was calculated using Fukui's formalism, $\mathbf{F}(\mathbf{k}) \equiv \ln \left[U_1(\mathbf{k}) U_2(\mathbf{k} + \hat{1}) U_1(\mathbf{k} + \hat{2})^{-1} U_2(\mathbf{k})^{-1} \right]$, where $\hat{1}(\hat{2})$ denotes the reciprocal basis vector and $U_{1(2)}$ is a purposely defined U(1) link variable [3]. Chern number [4] showed, as expected, trivial dependence on magnetic configuration because CrI₃ is a magnetic topological insulator.

[1] P.-W. Ma and S. L. Dudarev, Constrained density functional for noncollinear magnetism, *Phys. Rev. B* **91**, 054420 (2015).

[2] E. Gordon, V. Mkhitaryan, H. Zhao, Y. Lee, and L. Ke, Magnetic interactions and spin excitations in van der waals ferromagnet, *Journal of Physics D: Applied Physics* **54**, 464001 (2021).

[3] T. Fukui, Y. Hatsugai, and H. Suzuki, Chern numbers in discretized brillouin zone: efficient method of computing (spin) hall conductances, *Journal of the Physical Society of Japan* **74**, 1674 (2005).

[4] Z. Li, Y. Han, and Z. Qiao, Chern number tunable quantum anomalous hall effect in monolayer transitional metal oxides via manipulating magnetization orientation, *Physical Review Letters* **129**, 036801 (2022).

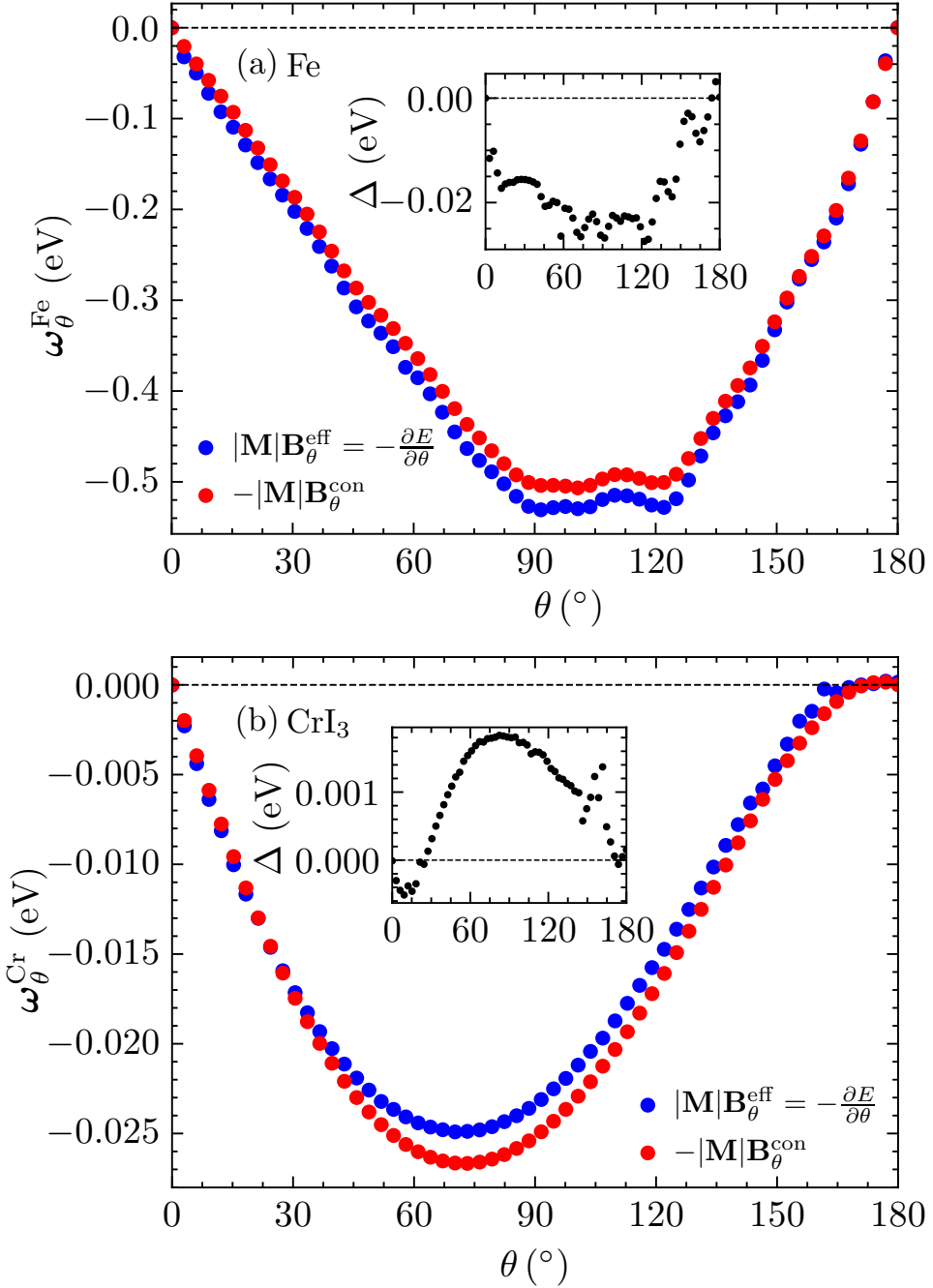
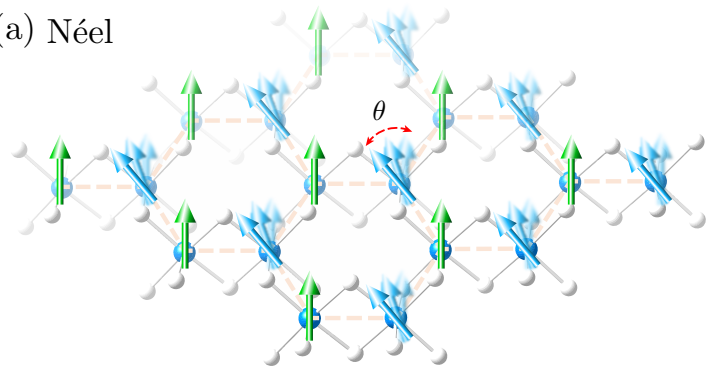
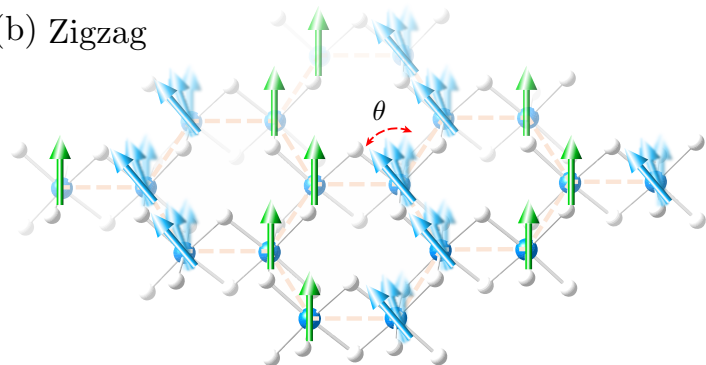


FIG. S2. Comparison of the magnetic torques calculated using finite difference $-\frac{\partial E}{\partial \theta}$ (blue scatters) and Hellmann–Feynman approximation $-|\mathbf{M}|\mathbf{B}_\theta^{\text{con}}$ (red scatters), respectively. The X axis represents the canting angle θ from ferromagnetic (FM) order ($\theta = 0^\circ$) to anti-ferromagnetic (AFM) order ($\theta = 180^\circ$). Insets show the difference between them. (a) BCC Fe (b) Monolayer CrI₃. Here for CrI₃, $\theta = 180^\circ$ corresponds to Néel phase, one of a few AFM orders it has.

(a) Néel



(b) Zigzag



(c) Stripy

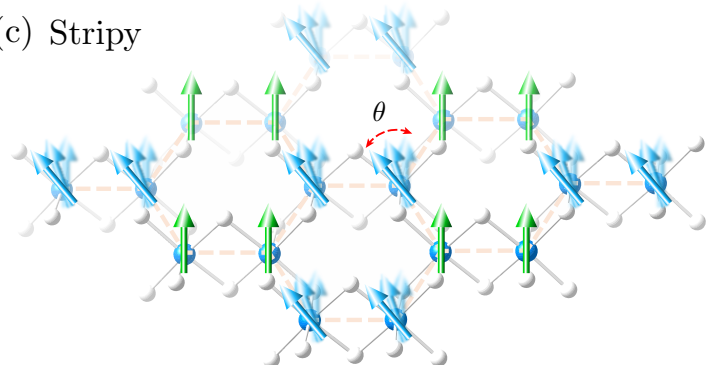


FIG. S3. Schematic of generalized Néel, Zigzag, Stripy AFM order in monolayer MX_3 . Blue spins cant at angle θ whereas green ones remain still. (a) Néel. (b) Zigzag. (c) Stripy.

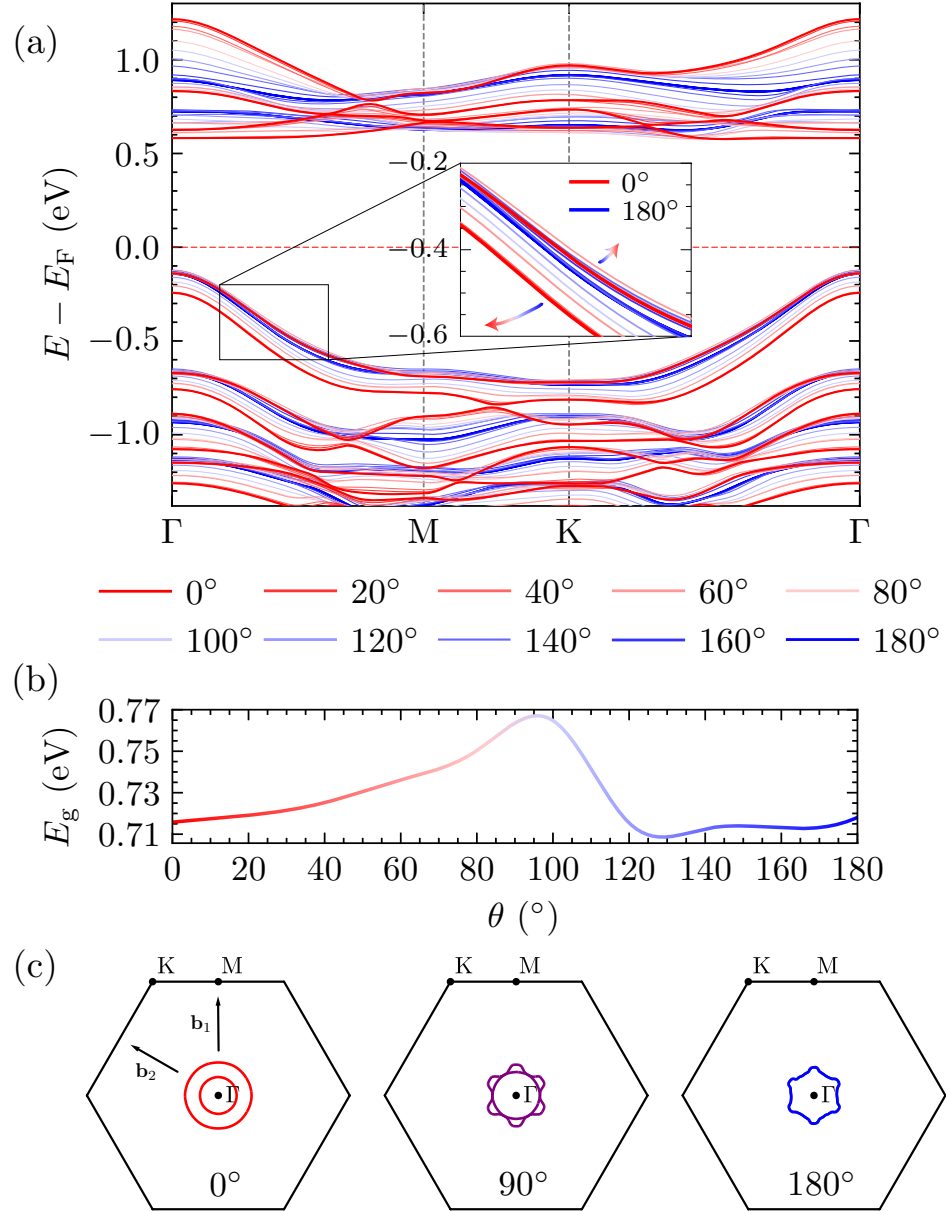


FIG. S4. Electronic structure of monolayer CrI_3 of different canting angles θ . (a) Band structure near Fermi level. Ten band structures are in the same figure, aligned according to their Fermi levels. The inset shows the two-fold splitting of VBM from FM phase (red, $\theta = 0^\circ$) to Néel AFM phase (blue, $\theta = 180^\circ$). (b) Band gap as a function of θ . (c) Fermi surface in two dimensions with $E = E_F - 0.31\text{eV}$. (d) Total Berry curvature and its gradient with respect to \mathbf{k} in reciprocal primitive cell at $\theta = 0^\circ, 90^\circ, 180^\circ$. (e) The derivative of Berry curvature with respect to θ as a function of \mathbf{k} in reciprocal primitive cell at $\theta = 0^\circ, 90^\circ, 180^\circ$.

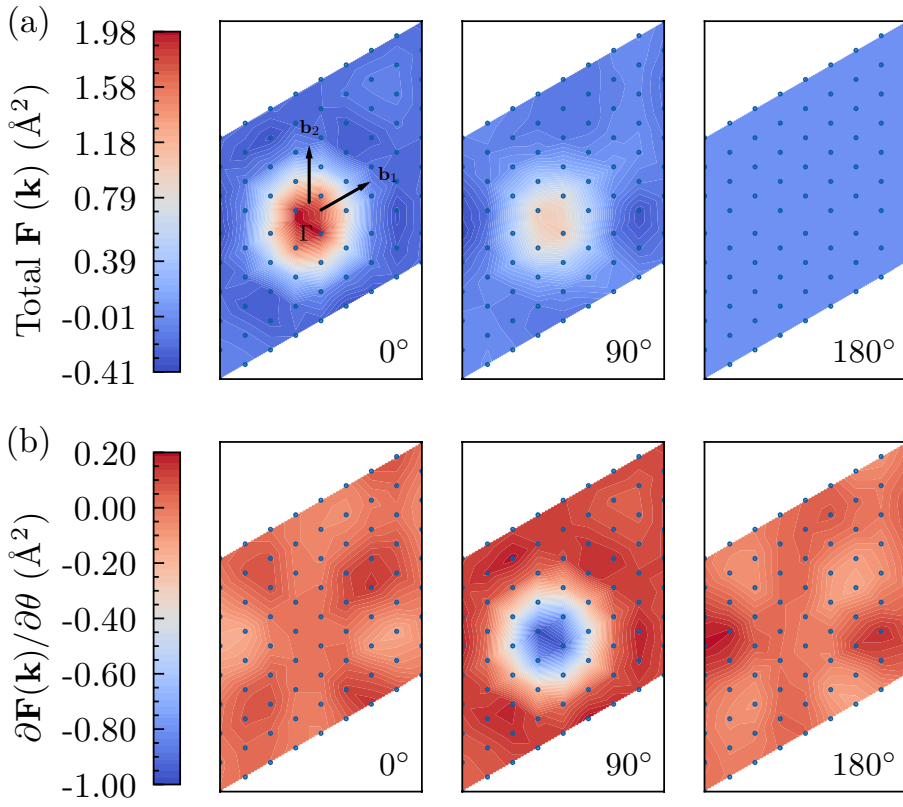


FIG. S5. Electronic structure of monolayer CrI₃ of different canting angles θ . (a) Total Berry curvature and its gradient with respect to θ as a function of \mathbf{k} in reciprocal primitive cell at $\theta = 0^\circ, 90^\circ, 180^\circ$. (b) The derivative of Berry curvature with respect to θ as a function of \mathbf{k} in reciprocal primitive cell at $\theta = 0^\circ, 90^\circ, 180^\circ$.